Check for updates

Polarization insensitive, metamaterial absorber-enhanced long-wave infrared detector

Chunxu Chen,[1] Yuwei Huang,[1] Ke Wu,[1] Thomas G. Bifano,[1,2] Stephan W. Anderson,[2,3] Xiaoguang Zhao,[1,3,4] (iD) and Xin Zhang[1,2,5] (iD)

[1]*Department of Mechanical Engineering, Boston University, Boston, Massachusetts 02215, USA*
[2]*Photonics Center, Boston University, Boston, Massachusetts 02215, USA*
[3]*Department of Radiology, Boston University Medical Campus, Boston, Massachusetts 02118, USA*
[4]*zhaoxg@bu.edu*
[5]*xinz@bu.edu*

Abstract: Detecting low energy photons, such as photons in the long-wave infrared range, is a technically challenging proposition using naturally occurring materials. In order to address this challenge, we herein demonstrate a micro-bolometer featuring an integrated metamaterial absorber (MA), which takes advantage of the resonant absorption and frequency selective properties of the MA. Importantly, our micro-bolometer exhibits polarization insensitivity and high absorption due to a novel metal-insulator-metal (MIM) absorber design, operating at 8-12 μm wavelength. The metamaterial structures we report herein feature an interconnected design, optimized towards their application to micro-bolometer-based, long-wave infrared detection. The micro-bolometers were fabricated using a combination of conventional photolithography and electron beam lithography (EBL), the latter owing to the small feature sizes within the design. The absorption response was designed using the coupled mode theory (CMT) and the finite integration technique, with the fabricated devices characterized using Fourier-transform infrared spectroscopy (FTIR). The metamaterial-based micro-bolometer exhibits a responsivity of approximately 198 V/W over the 8-12 μm wavelength regime, detectivity of $\sim 0.6 \times 10^9$ Jones, thermal response time of ~ 3.3 ms, and a noise equivalent temperature difference (NETD) of $\sim$33 mK under 1mA biasing current at room-temperature and atmosphere pressure. The ultimate detectivity and NETD are limited by Johnson noise and heat loss with thermal convection through air; however, further optimization could be achieved by reducing the thermal conductivity via vacuum packaging. Under vacuum conditions, the detectivity may be increased in excess of two-fold, to $\sim 1.5 \times 10^9$ Jones. Finally, an infrared image of a soldering iron was generated using a single-pixel imaging process, serving as proof-of-concept of this detection platform. The results presented in this work pave the road towards high-efficiency and frequency-selective detection in the long-wave infrared range through the integration of infrared MAs with micro-bolometers.

1. Introduction

Metamaterials, which represent a major class of artificially engineered electromagnetic (EM) composites, enable myriad extraordinary material properties. During the past decade, metamaterials have emerged as a focal point in the EM domain, given their capacity to enable the creation of novel effective optical properties, such as negative refractive index [1], giant circular dichroism [2–4], local field enhancement [5], and wave-front tuning [6–8], in the spectrum ranging from microwave [9] to infrared (IR) [10] and even visible wavelengths [11]. Metamaterials typically consist of periodically packed sub-wavelength unit cells, which serve to form a homogeneous effective response. By modifying the geometry or material properties at the unit cell level, the effective permittivity and permeability may be precisely controlled. As a result, metamaterials

have enabled many useful applications, including invisibility cloaking [12] and perfect absorption [13–15], among others. Recently, polarization sensitive metamaterials and metasurfaces have been developed to enable polarimetric imaging [16–19].

Micro-bolometers are a type of resistive electromagnetic detector [20] widely used in scientific, defense and industrial applications, due to their low weight, low power, high responsivity and stable long term operation compared to photonic-based detectors [21]. However, most practical, commercial infrared detectors, the application of interest herein, feature a broadband response and lack spectral selectivity [22]. Therefore, when micro-bolometer-based detectors require spectral selectivity, additional components must be added, such as fixed filters [23] and interferometers [24], leading to increasing cost and complications in device fabrication. Metamaterial absorbers (MA) offer an efficient solution to this problem. To date, metamaterial absorbers (MA) [25] have also attracted a great deal of interest as they yield a number of advantages for various applications such as energy harvesting [26], solar cells [27], and chemical sensing [28,29] due to the high absorption and large Q-factors of their structures. Importantly, the direct integration of metamaterial structures with infrared detectors such as micro-bolometers provides a route toward hyperspectral, ultra-sensitive imaging using a low cost, simple fabrication process [30–32].

In this paper, we demonstrate a metamaterial-enhanced micro-bolometer for detecting long-wave infrared (LWIR, 8-12μm) radiation. In contradistinction to prior efforts [33–36], our detector not only shows high spectral selectivity and polarization insensitivity, but also has an interconnected structure, which represents an ideal design for thermo-resistive-based detection. We extend the use of a metal/insulator/metal (MIM) structure as a mechanism for sensing in the LWIR domain based on the bolometric principle [37]. Our proposed detector incorporates both micro/nano-electromechanical systems (MEMS/NEMS) techniques and EM metamaterials structures. Due to the inherent properties of the MA, the metal-based structure yields a high degree of field concentration, reducing temperature fluctuation noise, lowering device capacitance and loss tangent noise, all of which are greatly beneficial to increasing the sensing performance of infrared detectors. Our device was initially designed using finite integration technique (FIT) simulations and the coupled mode theory (CMT), and experimentally characterized using Fourier transform infrared (FTIR) spectroscopy. Based on theoretical, simulation, and experimental results, our device achieves a narrowband (300 nm FWHM at 8.67 μm) but highly efficient (82%) absorption. Subsequently, a thorough analysis of our device performance was conducted, including thermal time constant (τ), responsivity (R_v), temperature coefficient of resistance (TCR) and detectivity (D^*) measurements. The noise equivalent power (NEP) and noise equivalent temperature difference (NETD) are also calculated at room temperature. Finally, the fabricated device was validated in an imaging platform using a custom-made set up, with single-pixel imaging of a soldering iron successfully performed. Our work outlines a readily feasible strategy towards hyperspectral, sensitive infrared detection, without the need for complex fabrication and strictly hermetic packaging.

2. Long-wave infrared detector design

The infrared detector consists of a MIM metamaterial absorber (MA)-enhanced sensing element suspended by supporting beams. In the design of the detector, we aimed to maximize the infrared absorption response and thermal resistive change to maximize performance. In order to maximize the absorption, an ideal MA should 'perfectly' absorb IR radiation given any polarization across a wide incident angle. To maximize the resistance of the thermal resistive detection and further enhance the detection performance, unit cells of the MA are interconnected in one direction (y-axis) and disconnected in the perpendicular direction (x-axis). Such design of metamaterials would maximize the effective length of the thermal resistor, thereby maximize the initial resistance and absolute resistance change for optimizing the responsivity. However, this asymmetry in the unit cell design yields a polarization-sensitive absorption response [38]. Therefore, as shown

in the inset of Fig. 1(a), we designed a unit cell featuring an interconnected cross and two side bars to achieve a polarization insensitive response in an asymmetric structure. The MA features a gold metamaterial structure on top, a PECVD silicon nitride (SiNx) spacer layer, and a gold mirror on the back. The cross structure absorbs the x-polarized incident energy while the side bars absorb the y-polarized incident energy. Therefore, the proposed MA structure is capable of achieving a high degree of polarization insensitive absorption at the designed wavelength, such as in the long-wave infrared region with a peak wavelength approximating 9 μm as in the device designed and validated herein, which is at the infrared atmospheric window [39] and the peak of the blackbody spectrum for human body, potentiating the application to human imaging. In addition, we sought to optimize the thermal response in the detector. To this end, by etching the underlying silicon substrate and patterning the electric wires on the suspending beams in a meander line fashion, the thermal loss due to conduction is minimized, resulting in a higher responsivity.
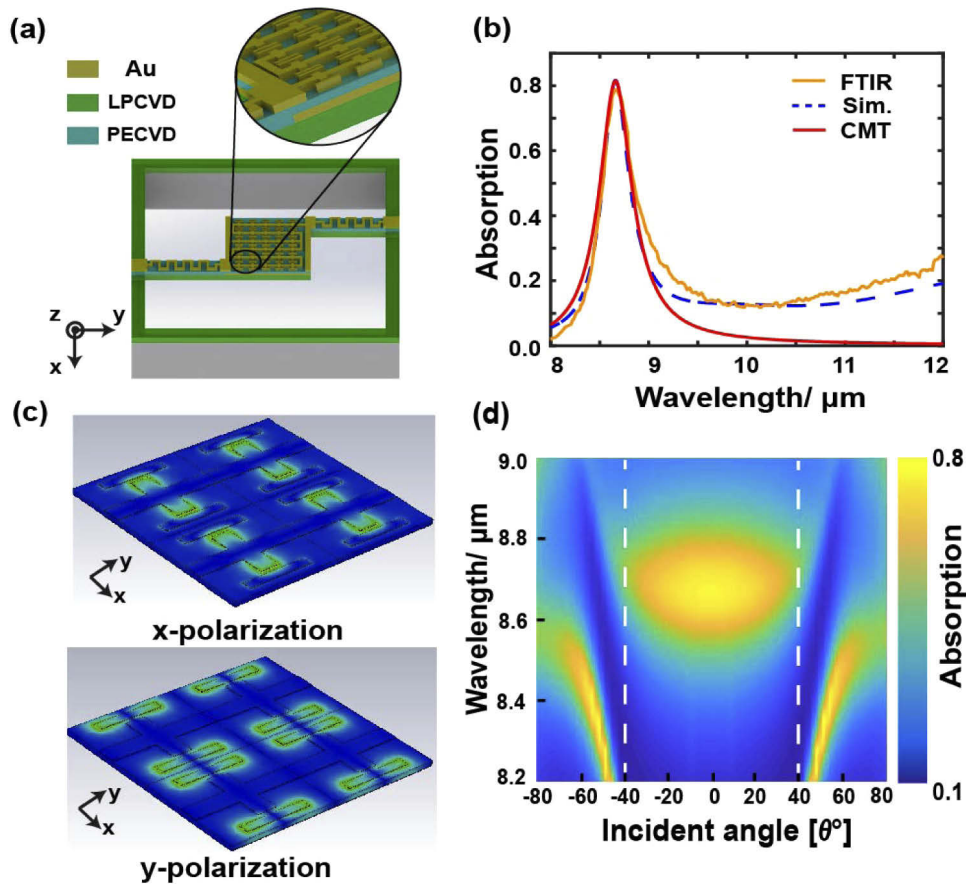

Fig. 1. (a) Schematic drawing of the infrared detector. The inset shows a close-up view of the MA structure. (b)-(d) EM response of the metamaterial-enhanced infrared detector. (b) FTIR measurement results (orange line), simulation results (dashed blue line) and CMT analysis (red line). (c) Electric field distribution at the absorption peak (∼8.67 μm) for x-polarization (top) and y-polarization (bottom). (d) Simulation results for angular absorption of the metamaterial-enhanced long-wave infrared detector. As shown within the white dashed lines, high absorption is achieved between −40° and 40° at ∼8.67 μm.

In order to quantitatively design the MA structure, an analytical model based on the coupled mode theory (CMT) was initially employed to study the absorption response. The theory describes the system with lumped parameters such as mode amplitudes, decay rates, and coupling coefficients [40–42]. In the MIM sensing component, the reflection coefficient can be expressed by the following equation:

$$r = -1 + \frac{1/Q_r}{-i(\omega/\omega_0 - 1) + 1/(2Q_a) + 1/(2Q_r)} \tag{1}$$

in which ω_0 is the resonance frequency, and Q_a and Q_r are the absorptive and radiative quality factors, respectively. The resonance frequency is determined by the metamaterial structure and Q_a (Q_r) is defined as the ratio of stored (radiated) energy to the time-averaged energy within a single unit cell. Since the ground plane is employed to eliminate the transmission wave and the scattering induced by the subwavelength structure is negligible, the absorption is determined by $A = 1 - |r|^2$. The quality factors (Q_a and Q_r) determine the absorption amplitude and perfect absorption may be achieved when Q_a is equal to Q_r. In the case of a resonating MA, Q_a may be calculated by the ratio between the stored energy in the resonator and the Ohmic energy loss in each cycle, while Q_r is the ratio between the stored energy in the resonator and the radiative energy loss. These quality factors are a function of the geometry of the specific MA structure; in the case of complicated structures, their values may be obtained by fitting a numerically simulated response.

Finite integration technique (CST Microwave Studio) was employed to optimize the geometry of the MA. The unit cell boundary and normal incidence conditions were used in the numerical simulation over a frequency ranging from 24 to 38 THz. In the long-wave infrared regime, it is well known that gold should be considered with the Drude model. Here, the dispersion relation of gold is obtained by fitting Ward's experimental data [43] with a plasma frequency of 2175 THz and collision frequency of 6.5 THz. As for silicon nitride, the Maxwell-Helmholtz-Drude dispersion model and the multiple reflection model are used to extract the permittivity of SiNx. Details regarding the extraction procedure and extracted permittivity may be found in our previous work [44] and Appendix A. By optimizing the MA geometry, near perfect absorption at the resonance frequency may be obtained. The overall absorption amplitude represents the averaged absorption for both x- and y-polarization directions. The calculated absorption spectra for x- and y-polarization directions are shown and discussed in Appendix B. The resonance frequencies are within close proximity to one another, resulting in a high degree of absorption for incident waves with arbitrary polarization or un-polarized incidence. The two quality factors, Q_a and Q_r, in the CMT are retrieved from the simulation results by the curve fitting method, the results of which are depicted in Fig. 1(b) with $Q_r \sim 29.3$ and $Q_a \sim 57.6$. Figure 1 also illustrates the fact that our MA design does not achieve perfect absorption (100% absorption), though in an underdamped condition.

The electric field distribution of the metamaterial structure at the resonance frequency is shown in Fig. 1(c). The dipole resonant modes for both x- and y-polarization directions are clearly presented in the E-field plot. As expected, for x-polarization, the dipole resonance primarily occurs at the cross-shaped structure, while for y-polarization, the dipole resonance is observed at the two separate bars.

Importantly, our proposed infrared detector also exhibits a high degree of absorption at the targeted wavelength over a wide angle of incidence, which will enable lower f-number and wide field of view (WFOV) within the thermal imaging applications. As can be seen from the FDTD simulation results in Fig. 1(d), the detector captures nearly 80% of the infrared radiation at ~8.67 μm between −40° to 40°. Beyond this critical angle (40°), due to the effective pattern period reduction in the unit cell structure and the coupling between elements, a redshift of the resonance is observed, most prominent with y-polarization.

3. Materials and methods

The metamaterial-enhanced infrared detector was fabricated using bulk micromachining processes, including electron beam lithography (EBL) and photolithography, as shown in Figs. 2(a)–2(f). The silicon wafer was first coated on both sides with low pressure chemical vapor deposited (LPCVD) silicon nitride. Next, the front side of the SiNx was selectively etched, and a gold ground plane was patterned using a lift-off process for the central sensing portion. Then, a plasma-enhanced chemical vapor deposited (PECVD) silicon nitride film was grown on top of the wafer as a spacer layer and selectively etched using reactive ion etching (RIE). Subsequently, the meander gold connection wires and the metamaterial structures were patterned using photolithography and EBL processes, respectively. Finally, in order to reduce the thermal loss through the silicon substrate, the entire detector structure was released with KOH wet etching and the silicon substrate was entirely removed. The unit cell structure of the proposed infrared detector is shown in Fig. 2(g); the periodicity (P) of the MA unit cell is 5.7 μm, while the line length for the cross-shaped structure and the separate bars are 1 μm (l_1) and 3.4 μm (l_2), respectively. The line widths of the
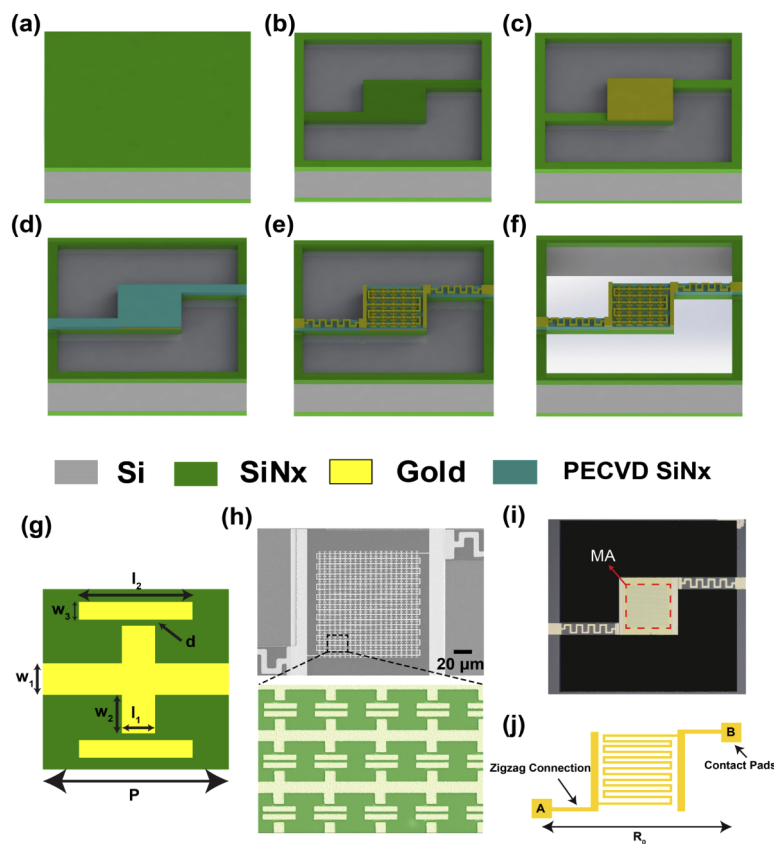

Fig. 2. (a-f) Process flow to fabricate metamaterial-enabled infrared detector. (g) Unit cell of the metamaterial-enabled infrared detector, including a cross-shaped structure and two separate bars. (h) SEM image of the fabricated detector before release (step e), entire structure (top) and close-up false color image (bottom). (i) Optical microscopic image of the final released structure; the silicon in the black area was etched away using potassium hydroxide (KOH) wet etching. The dashed red line shows the sensing part with MA structure. (j) Schematic of the sensing elements, in which the contact pads (A and B) are used for interfacing with external biasing current.

constituent components are 1 μm (w_1), 1.2 μm (w_2) and 0.5 μm (w_3). Of note, the metal coverage was only 34.5% for our metamaterial absorber design, markedly reducing the thermal mass and capacitance. Scanning electron microscopy (SEM) and optical microscopy (OM) images of the fabricated devices are shown in Figs. 2(f) and 2(i), respectively. The close-up false color image shows the metamaterial structure successfully fabricated with EBL and photolithography processes.

The EM absorption spectra of the IR detector was measured with an FTIR spectrometer (Vertex 70 V, Bruker Corp.), which was coupled to an infrared microscope (Hyperion 1000, Bruker) with a Cassegrain reflection optics objective (15 × with number aperture (NA): 0.4) and a liquid N_2 cooled mercury cadmium telluride (MCT) detector via a KBr beam splitter. The incident infrared light was defined using a knife edge aperture and illuminated on a 150 μm × 150 μm area on the detector. The measured reflectance was normalized with respect to a gold mirror with 95% reflectivity over 8-12 μm. The slight difference between the experimental and simulation results at the longer wavelengths is due to the fabrication defects and measurement errors within the FTIR measurement.

After the wafer-scale fabrication, the MIM sensing portion was electrically connected to the connection pads through meander gold connection beams on both sides, as shown in Fig. 2(j). In order to measure the resistance and output voltage change with increased temperature, a conductive silver epoxy was used to attach bonding wires to the contact pads and connected to the interfacial printed circuit board (PCB) for the electrical readout using a multi-meter (Keithley 2700 Multi-Meter) and a source-meter (Keithley 2400 Source-Meter). We characterized the thermal coefficient of resistance (TCR) by measuring the resistance of the detector under different temperatures, varied using a hot plate (Fisher-brand Iso-temp SP88857200).

4. Results and analyzation

As shown in Fig. 1(b), the absorption spectrum of our long-wave infrared detector is measured with FTIR under un-polarized light. The simulation results in Fig. 1(b) are based on the average of absorption power for both x- and y-polarization. The detailed EM simulation results of the detector for x- and y-polarization are shown in Appendix B.

After measuring the EM response of the metamaterial structure, the detector's thermal response and performance are further analyzed. The working principle of our metamaterial-enhanced micro-bolometer is based on the thermal resistive effect. Initially, the MA structure absorbs infrared radiation and directly converts the EM energy to heat. Next, heat increases the local temperature of the entire detector and induces a resistance change in the thermo-resistive layer, which is the top gold layer with the metamaterial patterns. Finally, the change in resistance of the detector is measured through a multi-meter with the help of DC biasing current. Notably, all of the measurements below were performed at room temperature without vacuum packaging. For micro-bolometers, in order to achieve higher responsivity, it is preferable to use an absorbed material with larger temperature coefficient of resistance (TCR). TCR is defined as the relative resistance derivative 1/R(dR/dT), which in turn manifests the resistance change factor per kelvin (K) [45]. Figure 3(a) exhibits the measured resistance and output voltage at an injection current of $I = 1$ *mA* with the temperature changing from room temperature (300 K) to 373 K. The measured TCR value approximates 0.0017, derived by fitting the blue line shown in Fig. 3(a). The responsivity wavelength of our bolometer-based infrared detector dependence is depicted in Fig. 3(b), demonstrating a high spectrally resolved detection. The responsivity (R_v) of an infrared detector is defined by the following expression [46]:

$$R_v = \frac{V_s}{\Phi_e(\lambda)} \tag{2}$$

where V_s is the signal voltage (V) due to Φ_e, and $\Phi_e(\lambda)$ is the radiant incident power (W). The calculated stationary responsivity at room temperature is obtained from the measured absorbance spectra (Fig. 1(b)), blackbody radiation calculation and the output voltage (Fig. 3(a)). From 8-12 μm, the overall responsivity is ~ 198 V/W, while the peak responsivity is ~ 23 V/W at 9 μm and nearly 30% of the radiation energy is absorbed between 8.5-9.5 μm, demonstrating the high spectral selectivity of our infrared detector.
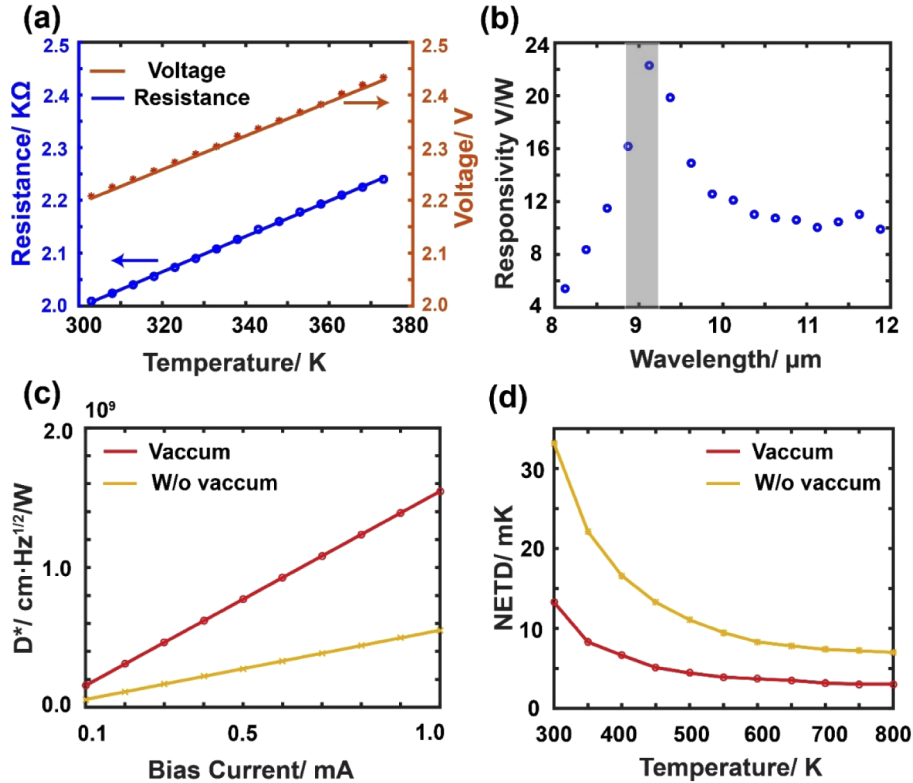

Fig. 3. Performance metrics of the infrared microbolometer. (a) The experimentally measured resistance change (blue line) and the detector's output voltage under 1 mA bias current (orange line). (b) Calculated responsivity wavelength dependence of the detector at room temperature. The peak responsivity is around 9 μm and the value is approximately 23 V/W within the shaded grey area. (c) Normalized detectivity (D^*) of the detector. Predicted D^* as a function of current under vacuum (red line) and predicted D^* without vacuum seal (yellow line). (d) Noise equivalent temperature difference (NETD) of the fabricated detector as a function of temperature. NETD with (red line) and without vacuum (yellow line).

Ultimately, the sensitivity of the detector is not merely determined by the responsivity, but is also related to the noise of the sensor, a measure of which may be calculated from its noise equivalent power (NEP). For a bolometer-based detector such as presented herein, the Brownian motion of metal electrons (Johnson noise) is the dominant source of noise within the sensing elements and is directly proportional to the square root of the resistance of the sensor [47]. The NEP of the sensor can be expressed with the following equation [48]:

$$NEP = \frac{V_N}{R_v} = \frac{\sqrt{4k_B TR\Delta f}}{R_v} \tag{3}$$

where V_N is the root mean square noise of the output voltage and R_v is the peak responsivity of the detector that we measured and calculated above. Based on Eq. (3) and the responsivity over 8-12 μm, the NEP of the detector is $\sim 29 \, pW/\sqrt{Hz}$.

Following the NEP calculation, the normalized detectivity (D^*) of the sensor is calculated with a bias current change from 0.1 mA to 1 mA. D^* is one of the most fundamental parameters in evaluating the performance of the sensor and is defined as the reciprocal of the NEP normalized by both the detector area (A) and electrical bandwidth (Δf) and expressed by the following equation [49]:

$$D^* = \frac{\sqrt{A\Delta f}}{NEP} \qquad (4)$$

As shown in Fig. 3(c), D^* of the detector was calculated using a COMSOL simulation model. The model was developed in order to solve for the thermal response and simulate the heat transfer processes of the detector, estimating the temperature change in the detector. The COMSOL model employed the geometric dimensions of the detector, the thermal and electrical constants of the materials and the incident radiation power at room temperature as the input parameters to calculate stationary D^* as a function of bias current. The incident radiation power is calculated by integrating the blackbody radiation of heat source and the absorption spectral of the detector. In the case of our infrared detector, D^* can achieve $\sim 0.6 \times 10^9 cmHz^{1/2}/W$ (Jones). Meanwhile, the thermal time constant (τ) of the device was also derived based on the COMSOL model with additional input parameters of the chopping frequency and the third harmonic of the detector's output voltage (with 3ω method) versus the modulation frequency [50]. As a result, the cut-off frequency of the detector was found to approximate 300 Hz, equivalent to a time constant of 3.3 ms. Details of the calculations and results may be found in Appendix C.

Finally, we estimated the noise equivalent temperature difference (NETD) of the detector. The NETD is defined as the minimum difference in temperature from the background that can be distinguished above the noise level, and corresponds to the resolution of the detector [51]. The NETD can be expressed with the following equation:

$$NETD = V_N \frac{\Delta T}{\Delta V} = \frac{\sqrt{4k_B TR\Delta f}}{\Delta V} \qquad (5)$$

where ΔT is the temperature difference for two given temperatures of the heat source and ΔV represents the output voltage difference induced from the ΔT. Here, we again employ the aforementioned COMSOL model to calculate the temperature change of the device surface with two different heat source temperatures, 300 K and 305 K. Based on the simulation results, a 5 K temperature difference in the heat source results in approximately a 0.002 K difference in temperature on the device surface, while inducing a 0.007Ω change based on the TCR relationship shown above. As shown in Fig. 3(d), the NETD approximates 33 mK at room temperature (300 K), which decreases to approximately 7 mK at 800 K; this decreasing trend is common in most bolometer-based infrared detectors.

The performance metrics of the detector could be further optimized with a reduction in thermal convection by integrating a partial vacuum packaging (pressure ~1 mbar). The vacuum seal would prevent heat transport via air and drastically improve the signal-to-noise ratio (SNR) of the presented metamaterial-enhanced infrared detector. As shown in Figs. 3(c) and 3(d), the normalized detectivity (D^*) increases to $\sim 1.5 \times 10^9 cmHz^{1/2}/W$ and the noise equivalent temperature difference (NETD) decreases from 33 mK to 13 mK at room temperature using a partial vacuum seal.

Subsequently, we imaged a soldering iron using our metamaterial-enhanced micro-bolometer, as shown in Fig. 4. The testing setup is shown in Fig. 4(a); the soldering iron on the left served as an infrared source and an infrared lens (operating wavelength range of 8-12 μm and focal length ~ 3 cm) in the middle served to focus the image onto our detector. We used an XYZ stage to scan

the infrared detector in a 3D fashion. Finally, the multi-meter on the right measured the resistance change (ΔR) at different locations (x-z plane). The final image is shown in Fig. 4(b), in which the black dashed line shows the outline of the soldering iron head. The resistance change can be directly converted to the temperature of the soldering iron and the detailed conversion results can be found in Appendix D. As shown in the single-pixel imaging, the tip of the soldering iron has the highest temperature (approximately 605 K based on the conversion equation) when compared with the upper portions of the iron. The absolute resistance change (ΔR) of the detector may be expressed by $\Delta R = b \times e^{(-(\alpha T - \beta)^2)}$, where b = 2.32, α = 2.64 × 10⁻³, and β = 2.52 that are obtained by fitting the simulation results. Since the resolution of the XYZ stage is limited and the position of the detector may deviate slightly from the focal plane of the IR lens, the final infrared imaging results are relatively blurred along the edges of the soldering iron. However, these results support the concept that metamaterial absorber-based IR detectors may be suitable for various practical applications, such as portable nondispersive infrared sensors (NDIR), chemical IR sensing, and thermography, among others.
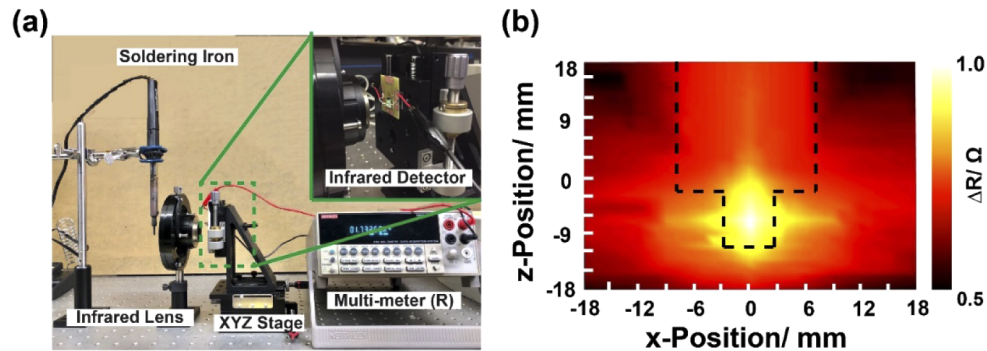

Fig. 4. (a) Testing setup for scanning the IR image of a soldering iron. (b) Soldering iron single pixel infrared image.

5. Conclusion

In summary, we present the design, fabrication, characterization and performance analysis of a metamaterial-enabled micro-bolometer and demonstrated its use in IR imaging. By integrating an MA structure with the micro-bolometer, polarization insensitive, spectrally-selective and high absorption sensing over 8-12 μm wavelength region without the need for any external filter or polarizer is realized. The MA structure uses a classical MIM layout and efficiently absorbs infrared radiation across a broad range of incident angles. The EM response of the metamaterial structure was analyzed using numerical simulation (CST Microwave Studio) and the coupled mode theory, and the device was characterized using FTIR. Near perfect absorption was confirmed with both simulation and experimental results at the resonant wavelength (~8.67 μm). After successfully assembling the MA and micro-bolometer structures, the performance metrics of the detector were experimentally measured and calculated in detail. Due to the intrinsic advantages of the MA structure, the proposed infrared detector shows a remarkable responsivity, NEP and NETD, without the use of vacuum packaging. Our initial study presented herein demonstrates the potential of integrating optical, thermal and electrical functions together into a single structure by utilizing metamaterial and micro-bolometer structures. Although in our proposed detector, the MA achieves high absorption only at MIR region, this may be readily tuned to address other frequencies of interest by simply changing the dimensions of the unit cell structures. The detector presented in this work offers a promising pathway towards hyperspectral focal plane array (FPA) systems and miniaturized nondispersive infrared sensors.

Appendix A: Retrieving permittivity of silicon nitride thin film

The permittivity of SiNx is extracted based on the curve fitting method and the Maxwell-Helmholtz-Drude dispersion and multiple reflection models. The permittivity of SiNx may be represented with following equation:

$$\varepsilon_{SiNx} = \varepsilon_\infty + \sum_{j=1}^{M} \frac{\Delta\varepsilon_j\omega_{T_j}^2}{\omega_{T_j}^2 - \omega^2 - i\omega\Gamma_j'(\omega)} \tag{6}$$

where M is the number of oscillators, $\varepsilon_\infty = \varepsilon_{M+1}$ represents the relative permittivity of higher lying transitions, $\Delta\varepsilon_j = \varepsilon_j - \varepsilon_{j+1}$ represents the difference in relative complex dielectric constant between adjacent oscillators, which also serves as a measure of the oscillator strength, and ω_{T_j} is the resonance frequency of the jth oscillator. The effective Lorentzian damping coefficient, Γ_j' for $j = 1, \ldots, M$ may be calculated with the following functional form:

$$\Gamma_j'(\omega) = \Gamma_j \exp\left[-\alpha_j\left(\frac{\omega_{T_j}^2 - \omega^2}{\omega\Gamma_j}\right)^2\right] \tag{7}$$

where α_j represents the interpolation between Lorentzian ($\alpha_j = 0$) and Gaussian wings ($\alpha_j > 0$).

The reflection spectra of the SiNx thin film is shown in Fig. 5(a); the red line represents the FTIR measurement results, while the dashed blue line is the fitting curve using the parameters listed in Table 1. The extracted permittivity is shown in Fig. 5(b).
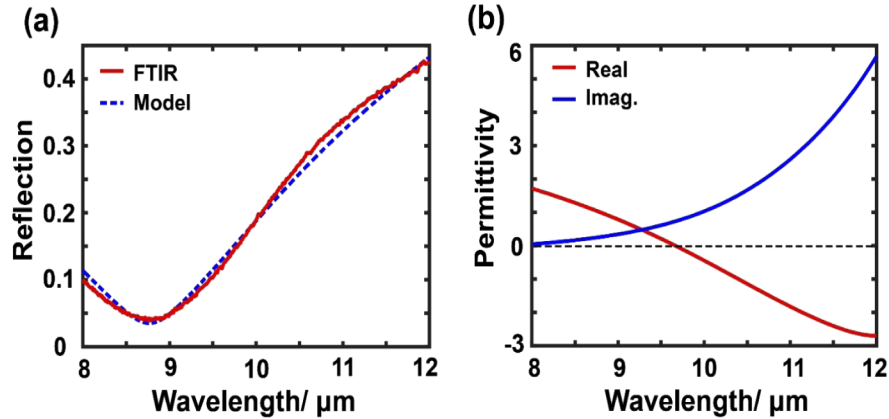

Fig. 5. (a) FTIR measurement (red line) and curve fitting (dashed blue line) results of a free-standing SiNx thin film with the identical thickness (0.4 μm) and optical properties as the nitride spacer layer used in the sensing component of the detector. (b) Retrieved permittivity of the SiNx thin film.

Table 1. Fitting parameters of the LPCVD grown SiNx thin film with $M = 5$.

j_h	$\varepsilon_j'(real)$	$\varepsilon_j''(imag)$	$\omega_{T_j}(THz)$	$\Gamma_j(THz)$	α_j
1	8.882	0	101.418	19.005	0.008
2	6.854	0.2359	105.581	20.439	0.100
3	6.401	0.0041	142.780	25.985	0.006
4	4.690	0.1779	130.827	108.154	1.800
5	3.582	0.3500	220.328	305.272	0.600
6	3.984	0.001			

Appendix B: EM response for x- and y-polarization

As shown in Fig. 6, the EM response of the MA may be described with the Jones vector and reflection matrix R [52]. For our current measurement, the incident wave is an un-polarized light with $E_x = E_y$. Consequently, the overall absorption may be described as the average power of x- and y-polarization.

Appendix C: Calculation of thermal response time (τ)

The thermal response time (τ) is an important parameter of the infrared detector. The typical values of τ in a micro-bolometer working at room temperature range from approximately 0.5 ms to 1s [53]. In this paper, the thermal response time of our proposed detector is calculated using both numerical and COMSOL simulation models.

In terms of heat-transfer in thermodynamics, the total thermal conductance (G_{tot}) of the detector may be expressed with the following equation [54]:

$$G_{tot} = G_{cond} + G_{conv} + G_{radiation} \tag{8}$$

where G_{cond}, G_{conv} and G_{rad} are the thermal conductance of the total legs, heat convection from the pad, and heat radiation, respectively. By considering the geometry parameters and material properties of the proposed detector, the heat conduction via the beam (G_{cond}) is $\sim 3.2 \times 10^{-6} W/K$, the heat convection through the pad (G_{conv}) is $\sim 4.5 \times 10^{-6} W/K$, and the heat radiation (G_{rad}) is $\sim 2.8 \times 10^{-7} W/K$.

The thermal capacitance of the infrared detector is defined as follows:

$$C_{tot} = V_{SiNx} \times c_{SiNx} \times \rho_{SiNx} + V_{gold} \times c_{gold} \times \rho_{gold} \tag{9}$$

where c, ρ, and V are specific heat, density and volume of the material of interest, respectively. The total thermal capacitance of the detector is $\sim 2.5 \times 10^{-8} J/K$. As a result, the thermal response time constant $\tau = C/G \sim 3.25$ ms.
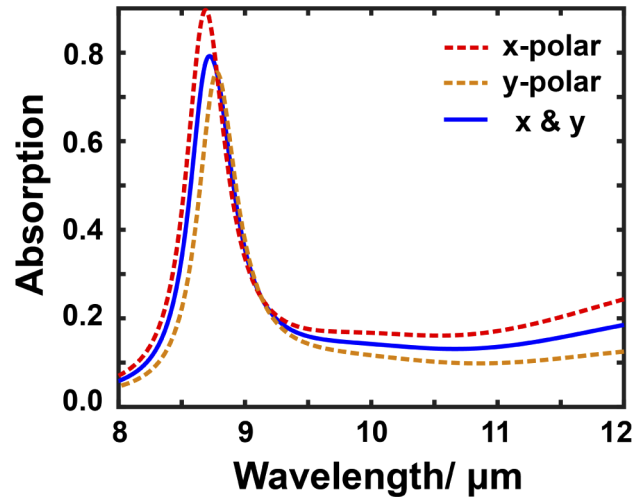

Fig. 6. EM response of the metamaterial absorber-enhanced long-wave infrared detector; the dashed lines show the simulated x- (red) and y- (orange) polarization, respectively, while the solid blue line shows the average of power for both polarization directions from simulation. All dimension parameters used in simulation are from the fabricated detector. The slight differences between the peak frequency of x- and y-polarization are due to imperfections in the fabrication process.

As shown in Fig. 7, the thermal response time is also calculated using the COMSOL simulation model. The model takes into consideration the geometry and constituent material properties as in the numerical calculation, while deriving the frequency response with a frequency domain perturbation study. Based on the AC electrical 3ω method [55], a 3 dB response time of ~ 3.3 ms is calculated, which is consistent with our numerical calculation.
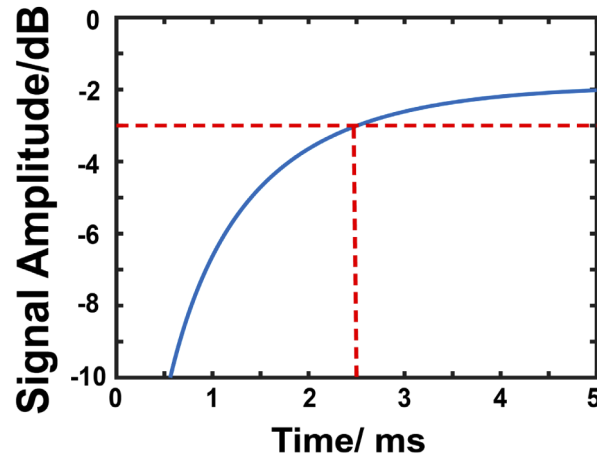

Fig. 7. Simulated detector frequency response. The cut-off frequency is ~ 300 Hz and the thermal response time is ~ 3.3 ms using the AC electrical 3ω method.

Appendix D: Relation between ΔR (Ω) and T (K)

As shown in Fig. 8, the conversion equation between the resistance change (ΔR) and the infrared source temperature (T) can be obtained by fitting the red curve. The simulation results are based
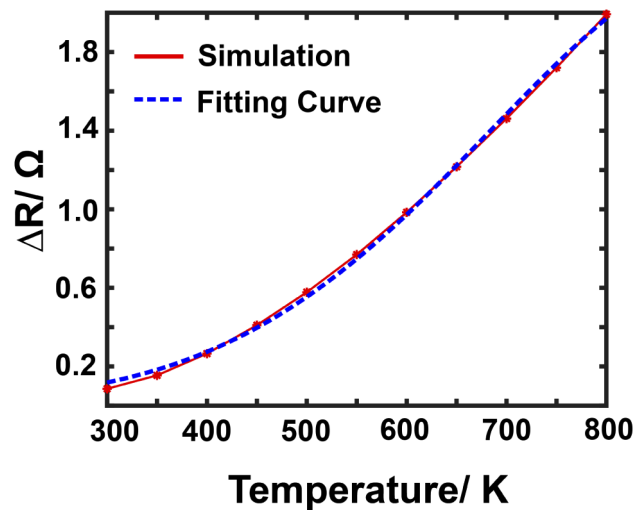

Fig. 8. Relationship between the resistance change of the detector (ΔR) and the infrared source temperature (T). The red line shows the simulation results for twelve temperature points from 300 K to 800 K, while the dashed blue line shows the fitting curve, with the equation $\Delta R = b \times e^{(-(\alpha T - \beta)^2)}$ Ω, where b $= 2.32$, $\alpha = 2.64 \times 10^{-3}$, and $\beta = 2.52$.

on the TCR value and heat transfer process of the detector. We simulated twelve different source temperatures, the results of which are shown with asterisks in Fig. 8.

Disclosures

The authors declare that there are no conflicts of interest related to this article.

References

1. R. A. Shelby, D. R. Smith, and S. Schultz, "Experimental verification of negative index of refraction," Science **292**(5514), 77–79 (2001).
2. M. Schäferling, D. Dregely, M. Hentschel, and H. Giessen, "Tailoring enhanced optical chirality: Design principles for chiral plasmonic nanostructures," Phys. Rev. X **2**, 31010 (2012).
3. E. Plum, J. Zhou, J. Dong, V. A. Fedotov, T. Koschny, C. M. Soukoulis, and N. I. Zheludev, "Metamaterial with negative index due to chirality," Phys. Rev. B **79**(3), 035407 (2009).
4. S. Zhang, Y. S. Park, J. Li, X. Lu, W. Zhang, and X. Zhang, "Negative refractive index in chiral metamaterials," Phys. Rev. Lett. **102**(2), 023901 (2009).
5. C. Ciracì, R. T. Hill, J. J. Mock, Y. Urzhumov, A. I. Fernández-Domínguez, S. A. Maier, J. B. Pendry, A. Chilkoti, and D. R. Smith, "Probing the ultimate limits of plasmonic enhancement," Science **337**(6098), 1072–1074 (2012).
6. S. Sun, Q. He, S. Xiao, Q. Xu, X. Li, and L. Zhou, "Gradient-index meta-surfaces as a bridge linking propagating waves and surface waves," Nat. Mater. **11**(5), 426–431 (2012).
7. H. T. Chen, A. J. Taylor, and N. Yu, "A review of metasurfaces: physics and applications," Rep. Prog. Phys. **79**(7), 076401 (2016).
8. A. M. H. Wong and G. V. Eleftheriades, "Perfect anomalous reflection with a bipartite huygens' metasurface," Phys. Rev. X **8**(1), 011036 (2018).
9. G. Duan, X. Zhao, S. W. Aderson, and X. Zhang, "Boosting magnetic resonance imaging signal-to-noise ratio using magnetic metamaterials," Commun. Phys. **2**(1), 35 (2019).
10. X. Liu, T. Starr, A. F. Starr, and W. J. Padilla, "Infrared spatial and frequency selective metamaterial with near-unity absorbance," Phys. Rev. Lett. **104**(20), 207403 (2010).
11. R. Maas, J. Parsons, N. Engheta, and A. Polman, "Experimental realization of an epsilon-near-zero metamaterial at visible wavelengths," Nat. Photonics **7**(11), 907–912 (2013).
12. P. Chen, J. Soric, and A. Alù, "Invisibility and cloaking based on scattering cancellation," Adv. Mater. **24**(44), OP281–OP304 (2012).
13. M. Wu, X. Zhao, J. Zhang, J. Schalch, G. Duan, K. Cremin, R. D. Averitt, and X. Zhang, "A three-dimensional all-metal terahertz metamaterial perfect absorber," Appl. Phys. Lett. **111**(5), 051101 (2017).
14. H. Tao, C. M. bingham, A. C. Strikwerda, D. Pilon, D. Shrekenhamer, N. I. Landy, K. Fan, X. Zhang, W. J. Padilla, and R. D. Averitt, "Highly flexible wide angle of incidence terahertz metamaterial absorber: Design, fabrication and characterization," Phys. Rev. B **78**(24), 241103 (2008).
15. X. Liu, K. Fan, I. V. Shadrivov, and W. J. Padilla, "Experimental realization of a terahertz all-dielectric metasurface absorber," Opt. Express **25**(1), 191–201 (2017).
16. L. Kang, S. P. Rodrigues, M. Taghinejad, S. Lan, K. Lee, Y. Liu, D. H. Werner, A. Urbas, and W. Cai, "Preserving spin states upon reflection: linear and nonlinear response of chiral meta-mirror," Nano Lett. **17**(11), 7102–7109 (2017).
17. A. Basiri, X. Chen, J. Bai, P. Amrollahi, J. Carpenter, Z. Holman, C. Wang, and Y. Yao, "Nature-inspired chiral metasurfaces for circular polarization detection and full-Stokes polarimetric measurements," Light: Sci. Appl. **8**(1), 78 (2019).
18. N. A. Rubin, G. D'Aversa, P. Chevalier, Z. Shi, W. Chen, and F. Capasso, "Matrix Fourier optics enables a compact full-Stokes polarization camera," Science **365**(6448), eaax1839 (2019).
19. Z. Wang, H. Jia, K. Yao, W. Cai, H. Chen, and Y. Liu, "Circular dichroism metamirrors with near-perfect extinction," ACS Photonics **3**(11), 2096–2101 (2016).
20. F. Niklaus, C. Vieider, and H. Jakobsen, "MEMS-based uncooled infrared bolometer arrays-A review," Proc. SPIE **6836**, 68360D (2007).
21. A. Rogalski, M. kopytko, and P. Martyniuk, *Antimonide-based infrared Detectors: A New Perspective* (SPIE, 2018).
22. J. Y. Suen, K. Fan, J. Montoya, C. Bingham, V. Stenger, S. Sriram, and W. J. Padilla, "Multifunctional metamaterial pyroelectric infrared detectors," Optica **4**(2), 276–279 (2017).
23. D. G. Manolakis, S. E. Golowich, and R. S. Dipietro, "Long-wave infrared hyperspectral remote sensing of chemical clouds," IEEE Signal Proc. Mag. **31**(4), 120–141 (2014).

24. P. G. Lucey, K. A. Horton, and T. Williams, "Performance of a long wave infrared hyperspectral imager using a sagnac interferometer and an uncooled microbolometer array," Appl. Opt. **47**(28), F107–F113 (2008).

25. C. M. Watts, X. Liu, and W. J. Padilla, "Metamaterial electromagnetic wave absorbers," Adv. Mater. **24**(23), OP98–OP120 (2012).

26. Z. Chen, B. Guo, Y. Yang, and C. Cheng, "Metamaterials-based enhanced energy harvesting: A review," Phys. B (Amsterdam, Neth.) **438**, 1–8 (2014).

27. Y. Wang, T. Sun, T. Paudel, Y. Zhang, Z. Ren, and K. Kempa, "Metamaterial-plasmonic absorber structure for high efficiency amorphous silicon solar cells," Nano Lett. **12**(1), 440–445 (2012).

28. X. Hu, G. Xu, L. Wen, H. Wang, Y. Zhao, Y. Zhang, D. R. S. Cumming, and Q. Chen, "Metamaterial absorber integrated microfluidic terahertz sensors," Laser Photonics Rev. **10**(6), 962–969 (2016).

29. N. Liu, M. Mesch, T. Weiss, M. Hentschel, and H. Giessen, "Infrared perfect absorber and its application as plasmonic sensor," Nano Lett. **10**(7), 2342–2348 (2010).

30. M. Mahjouri-Samani, Y. S. Zhou, X. N. He, W. Xiong, P. Hilger, and Y. F. Lu, "Plasmonic-enhanced carbon nanotube infrared bolometers," Nanotechnology **24**(3), 035502 (2013).

31. F. B. P. Niesler, J. K. gansel, S. Fischbach, and M. Wegener, "Metamaterial metal-based bolometers," Appl. Phys. Lett. **100**(20), 203508 (2012).

32. A. Safaei, S. Chandra, M. W. Shabbir, M. N. Leuenberger, and D. Chanda, "Dirac plasmon-assisted asymmetric hot carrier generation for room-temperature infrared detection," Nat. Commun. **10**(1), 3498 (2019).

33. F. Cheng, X. Yang, and J. Gao, "Ultrasensitive detection and characterization of molecules with infrared plasmonic metamaterials," Sci. Rep. **5**(1), 14327 (2015).

34. K. Chen, R. Adato, and H. Altug, "Dual-band perfect absorber for multispectral plasmon-enhanced infrared spectroscopy," ACS Nano **6**(9), 7998–8006 (2012).

35. S. Cataldo, J. Zhao, F. Neubrech, B. Frank, C. Zhang, P. V. Baraun, and H. Giessen, "Hole-mask colloidl nanolithography for large-area low-cost metamaterials and antenna-assisted surface-enhanced infrared absorption substrates," ACS Nano **6**(1), 979–985 (2012).

36. I. J. Luxmoore, P. Q. Liu, P. Li, J. Faist, and G. R. Nash, "Graphene-metamaterial photodetectors for integrated infrared sensing," ACS Photonics **3**(6), 936–941 (2016).

37. F. Simoens, M. Perenzoni, and D. Paul, *Physics and Applications of Terahertz Radiation* (Springer, 2014).

38. Z. Zhou, T. Zhou, S. Zhang, Z. Shi, Y. Chen, W. Wan, X. Li, X. Chen, S. N. Gilbert Corder, Z. Fu, L. Chen, Y. Mao, J. Cao, F. G. Omenetto, M. Liu, H. Li, and H. Tao, "Multicolor T-Ray imaging using multispectral metamaterials," Adv. Sci. **5**(7), 1700982 (2018).

39. S. Raghavan, D. Forman, P. Hill, N. R. Weisse-Bernstein, G. von Winckel, P. Rotella, and S. Krishna, "Normal-incidence InAs/In0.15Ga0.85As quantum dots-in-a-well detector operating in the long-wave infrared atmospheric window," J. Appl. Phys. **96**(2), 1036–1039 (2004).

40. G. Duan, J. Schalch, X. Zhao, A. Li, C. Chen, R. D. Averitt, and X. Zhang, "A survey of theoretical models for terahertz electromagnetic metamaterial absorbers," Sens. Actuators, A **287**, 21–28 (2019).

41. C. Qu, S. Ma, J. Hao, M. Qiu, X. Li, S. Xiao, Z. Miao, N. Dai, Q. He, S. Sun, and L. Zhou, "Tailor the functionalities of metasurfaces based on a complete phase diagram," Phys. Rev. Lett. **115**(23), 235503 (2015).

42. X. Zhao, Y. Wang, J. Schalch, G. Duan, K. Cremin, J. Zhang, C. Chen, R. D. Averitt, and X. Zhang, "Optically modulated ultra-broadband all-silicon metamaterial terahertz absorbers," ACS Photonics **6**(4), 830–837 (2019).

43. M. A. Ordal, L. L. Long, R. J. Bell, S. E. Bell, R. R. Bell, R. W. Alexander, and C. A. Ward, "Optical properties of the metals Al, Co, Cu, Au, Fe, Pb, Ni, Pd, Pt, Ag, Ti, and W in the infrared and far infrared," Appl. Opt. **22**(7), 1099 (1983).

44. X. Zhao, C. Chen, A. Li, G. Duan, and X. Zhang, "Implementing infrared metamaterial perfect absorbers using dispersive dielectric spacers," Opt. Express **27**(2), 1727–1739 (2019).

45. Y. Deng, S. F. Tang, H. Y. Zeng, Z. Y. Wu, and D. K. Tung, "Experiments on temperature changes of microbolometer under blackbody radiation and predictions using thermal modeling by COMSOL multiphysics simulator," Sensors **18**(8), 2593 (2018).

46. A. S. Ahmed, H. J. Kim, J. Kim, K. S. Hwang, and S. Kim, "Enhancing the responsivity of uncooled infrared detectors using plasmonics for high-performance infrared spectroscopy," Sensors **17**(4), 908 (2017).

47. A. Daniels, *Field Guide to Infrared Systems, Detectors, and FPAs* (SPIE, 2018).

48. A. Varpula, A. V. Timofeev, A. Shchepetov, K. Grigoras, J. Hassel, J. Ahopelto, M. Ylilammi, and M. Prunnila, "Thermoelectric thermal detectors based on ultra-thin heavily doped single-crystal silicon membranes," Appl. Phys. Lett. **110**(26), 262101 (2017).

49. S. Nudelman, "The detectivity of infrared photodetectors," Appl. Opt. **1**(5), 627–636 (1962).

50. A. Safaei, S. Modak, J. Lee, S. Chandra, D. Franklin, A. V. Guardado, and D. Chanda, "Multi-spectral frequency selective mid-infrared microbolometers," Opt. Express **26**(25), 32931–32940 (2018).

51. X. Xue, H. Xiong, Z. Song, Y. Du, D. Wu, L. Pan, and Z. Wang, "Silicon diode uncooled FPA with three-dimensional intergrated CMOS readout circuits," IEEE Sens. J. **19**(2), 426–434 (2019).

52. X. Zhao, J. Schalch, J. Zhang, H. R. Seren, G. Duan, R. D. Averitt, and X. Zhang, "Electromechanically tunable metasurface transmission waveplate at terahertz frequencies," Optica **5**(3), 303–310 (2018).

53. U. Dillner, E. Kessler, and H. G. Meyer, "Figures of merit of thermoelectric and bolometric thermal radiation sensors," J. Sens. Sens. Syst. **2**(1), 85–94 (2013).

54. F. Niklaus, C. Jansson, A. Decharat, J. Källhammer, H. Pettersson, and G. Stemme, "Uncooled infrared bolometer arrays operating in a low to medium vacuum atmosphere: performance model and tradeoffs," Proc. SPIE **6542**, 65421M (2007).

55. M. Ou-Yang, C. S. Sheen, and J. S. Shie, "Parameter extraction of resistive thermal microsensors by AC electrical method," IEEE Trans. Instrum. Meas. **47**(2), 403–408 (1998).